Nano Energy 81 (2021) 105664

Contents lists available at ScienceDirect

Nano Energy

journal homepage: http://www.elsevier.com/locate/nanoen

Full paper

Decorating vertically aligned MoS_2 nanoflakes with silver nanoparticles for inducing a bifunctional electrocatalyst towards oxygen evolution and oxygen reduction reaction

Getachew Solomon [a], Mojtaba Gilzad Kohan [a], Mikhail Vagin [b], Federica Rigoni [c], Raffaello Mazzaro [d], Marta Maria Natile [e], Shujie You [a], Vittorio Morandi [d], Isabella Concina [a], Alberto Vomiero [a,c,*]

[a] Division of Materials Science, Department of Engineering Sciences and Mathematics, Luleå University of Technology, SE-97187 Luleå, Sweden
[b] Department of Science and Technology, Laboratory of Organic Electronics, Linköping University, SE-601 74 Norrköping, Sweden
[c] Department of Molecular Sciences and Nanosystems, Ca'Foscari University of Venice, Via Torino 155, 30172 Venezia Mestre, Italy
[d] CNR-Institute of Microelectronics and Microsystem (IMM), Section of Bologna Via Piero Gobetti 101, Bologna 40129, Italy
[e] Institute of Condensed Matter Chemistry and Technologies for Energy (ICMATE), National Research Council (CNR) and Department of Chemical Sciences, University of Padova, Via Francesco Marzolo, 1, 35131 Padova PD, Italy

ARTICLE INFO

Keywords:
Oxygen evolution reaction (OER)
Oxygen reduction reaction (ORR)
Electrocatalyst
Bifunctional catalyst
Magnetron co-sputtering

ABSTRACT

Catalysts capable of improving the performance of oxygen evolution reaction (OER) and oxygen reduction reactions (ORR) are essential for the advancement of renewable energy technologies. Herein, Ag-decorated vertically aligned MoS_2 nanoflakes are developed via magnetron co-sputtering and investigated as electrocatalyst towards OER and ORR. Due to the presence of silver, the catalyst shows more than 1.5 times an increase in the roughness-normalized rate of OER, featuring a very low Tafel slope (58.6 mv dec^{-1}), thus suggesting that the catalyst surface favors the thermodynamics of hydroxyl radical (OH•) adsorption with the deprotonation steps being the rate-determining steps. The improved performance is attributed to the strong interactions between OOH intermediates and the Ag surface which reduces the activation energy. Rotating ring disk electrode (RRDE) analysis shows that the net disk currents on the Ag-MoS_2 sample are two times higher at 0.65 V compared to MoS_2, demonstrating the co-catalysis effect of silver doping. Based on the rate constant values, Ag-MoS_2 proceeds through a mixed 4 electron and a 2 + 2 serial route reduction mechanism, in which the ionized hydrogen peroxide is formed as a mobile intermediate. The presence of silver decreases the electron transfer number and increases the peroxide yield due to the interplay of a 2 + 2 electron reduction pathway. A 2.5–6 times faster conversion rate of peroxide to OH^- observed due to the presence of silver, indicating its effective cocatalyst nature. This strategy can help in designing a highly active bifunctional catalyst that has great potential as a viable alternative to precious-metal-based catalysts.

1. Introduction

The rapid increase in industrialization and the human population has increased the energy demand of the society. Developing efficient renewable technology to minimize the dependence on carbon-based energy resources is highly needed. Proton exchange membrane fuel cell (PEMFC) is one of the promising electrochemical energy conversion devices that produce electrical energy via a chemical reaction between a fuel such as hydrogen and an oxidant, oxygen. In addition to the high cost of the catalyst, the sluggish kinetics of the oxygen reduction process becomes a barrier for commercializing PEMFCs. Electrolysis of water into hydrogen and oxygen is also one of the encouraging technologies that can minimize the use of energy sources with a high CO_2 fingerprint [1]. However, due to the need for very expensive catalysts, and due to the sluggish thermodynamic uphill reaction of the oxygen evolution reaction (OER), the overall water splitting efficiency is very low. In both fuel cells and water electrolysis, oxygen reduction reaction (ORR) and oxygen evolution reactions (OER) are the slowest processes, mainly due

* Corresponding author at: Division of Materials Science, Department of Engineering Sciences and Mathematics, Luleå University of Technology, SE-97187 Luleå, Sweden
E-mail address: alberto.vomiero@ltu.se (A. Vomiero).

https://doi.org/10.1016/j.nanoen.2020.105664
Received 29 July 2020; Received in revised form 23 November 2020; Accepted 5 December 2020
Available online 8 December 2020

to the need for a 4-electron transfer during the reduction/oxidation process [2–4]. To date, noble metals such as Pt, Ir, Ru, and Pd are the most known efficient electrocatalysts. However, their practical application is limited by their high cost and scarcity. Catalysts based on transition metal sulfides and phosphides are getting much attention [5,6]. These materials are cost-effective and are showing remarkable versatility for OER, ORR reactions, thanks to their high density of surface-active sites.

MoS_2 is one of the typical catalysts with a relatively high active site density on the edge rather than on the basal plane [7]. Several efforts have been done to increase the number of exposed active sites of MoS_2, such as heteroatom doping and formation of heterostructures, which result in an improved catalytic performance [8–11]. Recently the bifunctional properties of MoS_2 and MoS_2-based heterojunctions were revealed by different studies. Baoshan et al. demonstrated the bifunctional nature of Fe-doped MoS_2 nanosheets. Iron doping influences the synthesis process, and enhance the electronic structure of the composites at the atomic scale [8]. In recent works, 2D MoS_2 nanosheets doped by transition metals have been proposed as an effective and low-cost electrocatalyst for ORR due to their high density of reactive sites [11,12]. The main challenge of ORR in low-temperature fuel cells under alkaline media is the requirement of the direct 4 electron transfer process. Platinum group catalysts are capable of providing 4 electrons [13]. Silver is also another possible catalyst capable of reducing molecular oxygen into water (4 electron transfer) or to peroxide (2 electron transfer). Due to this ability, silver has been actively employed for oxygen reduction reaction (ORR) [14–18]. Also, recent studies showed that silver can be used as a dopant to improve the OER activity of catalysts [19]. For instance, a homogeneously distributed Ag dopant enhances the stability and the catalytic efficiency of CoOOH towards OER by forcing Co to have a higher oxidation state [20].

In this study, we have synthesized vertically aligned MoS_2 nanoflakes using Magnetron co-sputtering and simultaneously decorated it with silver nanoparticles to investigate their OER and ORR activity. We demonstrate that magnetron co-sputtering is a valuable method to effectively decorate the MoS_2 surface with metal atoms without affecting its structure during the crystal growth process. Also, co-sputtering can help in controlling the unwanted side reaction of the dopant with the main catalyst (MoS_2), usually happens in a hydrothermal synthesis which makes it difficult to understand the role of metal dopant [9]. Vertically aligned MoS_2 flakes can possess maximum exposed sites for catalytic activity. Furthermore, doping and/or decorating MoS_2 surfaces with transition metals are effective ways to generate high oxidation states of the metal catalyst, which can improve the performance of the catalyst [19]. Since metal sites with higher oxidation state are very active towards OER [21,22], the presence of silver can produce a synergistic effect on the catalytic activity of the composite by modulating Mo to a higher oxidation state. Additionally, Ag multifunctional catalytic properties allow MoS_2 to have a higher conversion rate of the ORR intermediates which proves that Ag nanoparticles can induce and boost the bifunctional properties MoS_2 for both OER and ORR.

2. Experimental section

2.1. Materials and synthesis

Molybdenum sulfide target, MoS_2, 99.95% pure, 3.00" diameter, and Silver target, Ag, 99.99% pure, 3.00" diameter from Kurt J Lesker Company Ltd were used. MoS_2 and Ag-MoS_2 were grown on the Nickel foam (NF), silicon wafer, and fluorine-doped tin oxide (FTO) conductive glass (TEC 15 from Pilkington) substrates using magnetron sputtering for 30 min. The deposition rate is around 0.5 nm/s, calculated by combining the deposition duration, cross section SEM and RBS analyses. Before deposition, Nickel foam was sequentially treated in 3 M HCl, acetone, ethanol, and water in the ultrasonic bath to remove the surface oxide layer. To enhance the homogeneity of the deposited films the samples were constantly rotating (5 rpm). For the co-deposition, both Ag and MoS_2 targets sputtering rates were controlled through the applied power. We optimized the Ag concentration after performing different trials. Lower and higher Ag concentration was used to test the morphology difference and catalytic activity of the as prepared catalyst. The substrates were heated at 200 °C during the deposition. Argon gas with a flow rate of 20 sccm was introduced during the deposition.

2.2. Materials characterization

The morphology of the as-synthesized catalyst was characterized by a ZEISS SIGMA VP Field Emission Scanning Electron Microscope (FE-SEM). High-Resolution Transmission electron microscope (HR-TEM) characterization was performed on an FEI Tecnai G20 equipped with EDAX Energy-dispersive X-ray spectroscopy (EDS) and Fischione STEM-HAADF detector. Further morphological characterization was carried out by using a Bruker Dimension ICON AFM in PeakForce-QNM operation mode with a SCANASYST-AIR silicon cantilever (Bruker, spring constant ~0.4 N/m, nominal tip radius ~2 nm). XRD was carried on the PANalytical Empyrean X-ray diffraction diffractometer with Cu Kα source. Raman spectra were conducted on Raman Spectrometry (Senterra Raman spectrometer from Bruker equipped with 532 nm laser for excitation) in the ambient environment. The power of the excitation laser is kept at 0.2 mW to avoid heating and oxidation effect. Rutherford backscattering spectrometry (RBS) was applied for compositional and depth profiling characterization, by using a 1.8 MeV $^4He^+$ beam in IBM geometry and with scattering angle $\theta = 160°$. The analysis was performed on samples deposited on silicon. RUMP code simulation was used for the analysis of the spectra. The film thickness was independently measured by using cross-sectional SEM and RBS for comparative purposes.

X-ray Photoelectron Spectra were recorded using a PerkinElmer PHI 5600 ci spectrometer with a standard Al−Kα source (1486.6 eV) working at 200 W and a pressure less than 7×10^{-7} Pa. The spectrometer was calibrated by assuming the binding energy (BE) of the Au $4f_{7/2}$ line to be 84.0 eV with respect to the Fermi level. Both extended (survey, 187.85 eV pass energy, 0.5 eV $step^{-1}$, 0.025 $s{\cdot}step^{-1}$) and detailed spectra (for Mo 3d, S 2p, Ag 3d, O 1s and C 1s, with 23.5 eV pass energy, 0.1 eV $step^{-1}$, 0.1$s{\cdot}step^{-1}$) were collected. The binding energies (BEs, standard deviation = ± 0.1 eV) were corrected for the charging effects by considering the adventitious C 1s line at 284.8 eV. The atomic percentage, after a Shirley type background subtraction [23], was evaluated by using the PHI sensitivity factor [24].

2.3. Electrochemical measurements

The OER measurement was performed in a common three-electrode configuration using ModuLab XM ECS potentiostat (Solartron Instrument). Saturated calomel electrode (SCE) and a Pt plate were used as the reference and counter electrodes, respectively. Catalyst sputtered on 1 cm^2 nickel foam was used as a working electrode. All electrochemical measurements were conducted in alkaline media (1 M KOH, pH 14) and the reported potential was calibrated to a reversible hydrogen electrode (RHE), using E (vs.RHE) = E (vs. SCE) + 0.059 × pH + 0.242 V. All electrochemical measurements were manually iR-corrected. Electrochemical impedance spectroscopy (EIS) was carried out by applying 10 mV AC perturbation in the frequency range from 100 kHz to 3mHz at 1.50 V (vs.RHE). Chronopotentiometry experiment at 1.55 V vs RHE was carried out for a stability tests.

The ORR measurement was recorded using a three-electrode method with catalyst deposited on a glassy carbon electrode (area A = 0.196 cm^2). Hg/Hg_2O electrode was used as a reference and a platinum wire as a counter electrode. To prepare catalyst slurries, 5 mg of scratched catalyst from the sputtered film on FTO were dispersed in a mixture of 3 ml of distilled water, 2 ml of isopropanol, and 25 μL of Nafion, finally

sonicated for 10 min and stirred in a magnetic stirrer for 30 min 10 μL of the diluted slurries were loaded on a rotating disk electrode (RDE) for measuring the ORR parameters. The mass loading of the catalyst was 20 $\mu g/cm^2$ [25] The scan rate was 20 mV s^{-1} and the rpm of the RDE was varied from 0 to 2500 rpm in 0.1 M KOH of electrolyte.

3. Result and discussions

3.1. Morphology characterization

MoS_2 and Ag-MoS_2 composites were synthesized by magnetron co-sputtering on Nickel foam and FTO substrate, which provides a repeatable and uniform synthesis method. Substrate effect on morphology and Ag concentration effect on morphology and catalytical activity is first checked (the result and discussions are available in ESI Fig. S1-S3). Indeed the result shows samples grown on Nickel foam and FTO substrates resulted in similar morphology. For MoS_2, an average layer thickness of 1 μm was deposited at 200 °C. The morphological and structural analysis of the optimized samples is illustrated in Fig. 1a, b (on FTO), and Fig. S4a-e. The formation of nanoflakes is evidenced by the FE-SEM images and confirmed by an atomic force microscope (AFM) deposited at the same time and experimental conditions.

The MoS_2 nanoflakes grow perpendicular to the substrate. Using peak force tapping high-resolution AFM imaging, we measured the height of the MoS_2 nanowalls to be 60–80 nm, while the height of the Ag-MoS_2 flakes is lower, around 40–60 nm, as shown by high-resolution 3D AFM images (Fig. 1a, b).

The difference in height scale is due to the different background subtraction. However, the film thickness for Ag-MoS_2 composites has increased compared to bare MoS_2. From the line profile, the diameter of the tubular structure is around 23 nm for MoS_2. Compared to MoS_2, the Ag-MoS_2 nanoflakes grown by co-sputtering are denser and more irregular in shape, due to the presence of silver, which forms clusters on the surface of the composites. These unique structures are beneficial to expose more active surface sites during the catalytic process. As revealed by the EDS mapping (Fig. S5) and by cross-sectional EDS mapping analysis (Fig. S6), a homogenous Ag distribution is observed in the composite sample (Ag-MoS_2). An additional high-resolution EDS elemental mapping is performed by scratching the powder from the thin film. As shown in Fig. S7, Silver is homogeneously distributed around and into the MoS_2 structure.

The nanoscale morphology and composition of the samples are further investigated by HR-TEM, whose results are displayed in Fig. 2(a-e). Both samples are characterized by similar morphology and display a typical MoS_2 crumpled structure. In both samples, the high magnification micrographs (Fig. 2c-d) display a lattice spacing of 0.63 nm, corresponding to the (002) plane of the hexagonal MoS_2, which is consistent with the interlayer spacing of MoS_2 [8] folded edges and wrinkles.

Additionally, randomly oriented reflections with a d-spacing equal to 0.26 nm can be recognized on the related FFT, pointing out that the as-synthesized MoS_2 is not completely crystalline, with crystal domains limited to few nanometers. The composition of the Ag-doped sample was analyzed by STEM-EDS mapping. Fig. 2e (bottom) reports a typical EDS spectrum registered on the Ag-MoS_2 sample. The Ag content ranges from 15% to 18% at. in the sample, with respect to the atomic content of Mo, and homogeneously distributed in the material, with no evidence of segregation nor formation of a new phase. From the EDS profile performed across nanoflakes (Fig. S8), Ag concentration is quite homogeneous in the sample, at the nanoscale, within a single flake. Ag concentration variations can be observed, where two or more flakes overlap as shown in the EDS spectra in Fig. S8. Sulfur content is observed to be sub-stoichiometric with respect to the Mo content, but the EDS quantification (Fig. 2 g and ESI Fig. S5.) is affected by large error due to the superposition of the Mo and S emission peaks. The Mo:S:Ag atomic ratio obtained by EDS is close to the result estimated from RBS characterization, as discussed later in the text.

The crystal structures of the Ag-MoS_2 and MoS_2 were characterized by powder X-ray diffraction (XRD) technique. To avoid problems associated with the porosity of the structure of Nickel foam (NF), the XRD characterization was conducted on FTO glass. As shown in Fig. 3a, XRD patterns of both samples are similar. The broad reflections observed at 13.2°, 33.8°, and 61.6° are consistent with the (002), (100) and (110) crystal planes of MoS_2, respectively. The as-grown MoS_2 nanoflakes in both samples confirm the presence of the hexagonal MoS_2 crystal phase based on the PDF Code #27–0319. The intense reflections at $2\theta = 26.5°$,

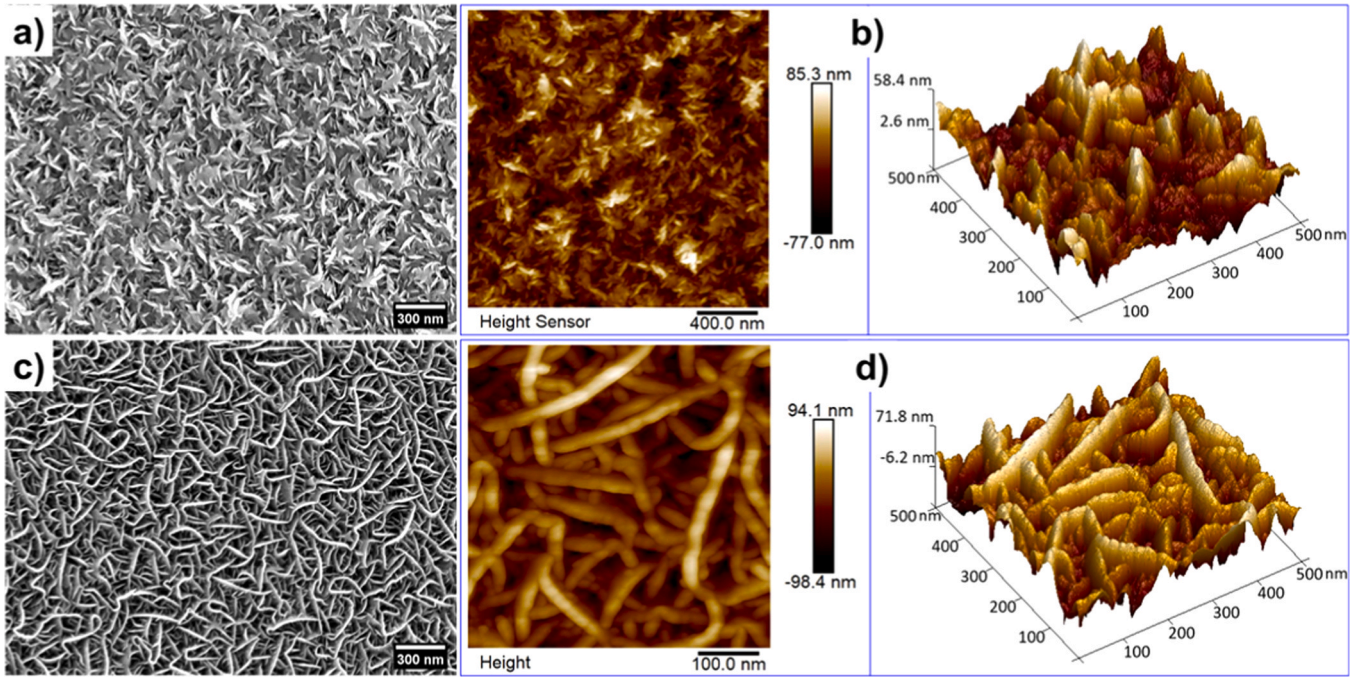

Fig. 1. FE-SEM and AFM images of Ag-MoS_2 (a, b) and MoS_2 (c,d), respectively.

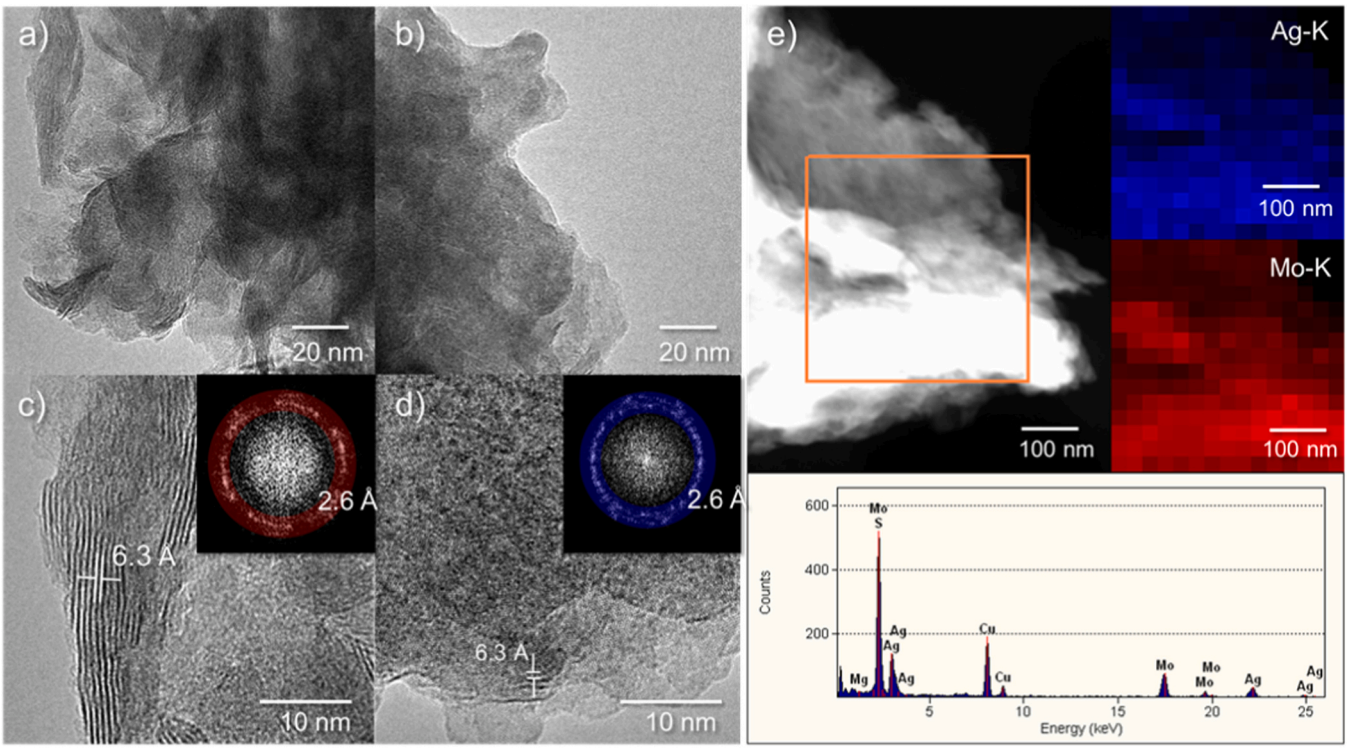

Fig. 2. (a, b) Low magnification and (c, d) high magnification HR-TEM micrograph of MoS_2 and Ag-MoS_2, respectively. In the inset, the relative Fast Fourier Transforms (FFT) are reported. e) STEM-HAADF micrograph of an Ag-MoS_2 nanoflake and relative EDS spectrum (bottom), in addition to the distribution of Ag and Mo content on the same flake (right), displayed as the intensity map of the related X-ray Kα peaks. The presence of Cu is associated with the TEM grid.

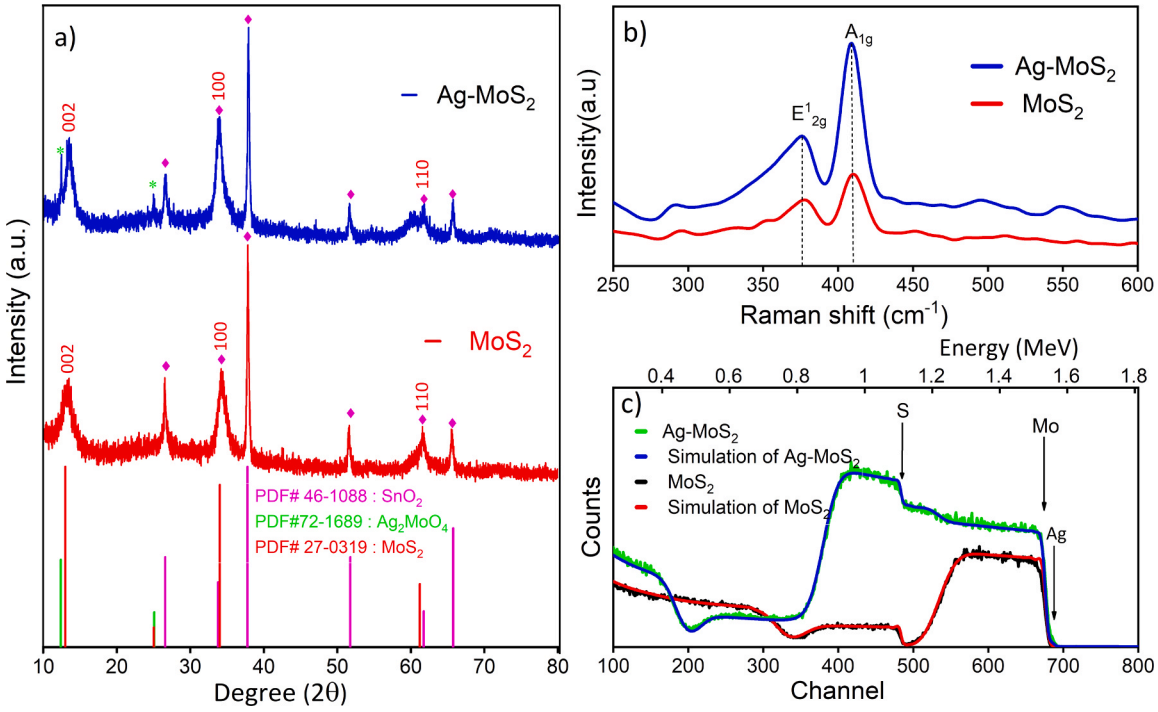

Fig. 3. (a) XRD and (b) Raman spectra of Ag-MoS_2 (blue) and MoS_2 (Red) respectively. In the bottom line of the panel (a) expected reflection patterns. (c) RBS spectra of Ag-MoS_2 and MoS_2 with associated x-RUMP code simulations. The surface edges for Ag, Mo, and S are indicated by the vertical arrows.(For interpretation of the references to colour in this figure legend, the reader is referred to the web version of this article.)

33.8°, 37.8°, 51.6°, and 65.6° are associated with FTO and indexed by PDF #46–1088. The very small contributions at 12.5°, 25° are associated with the formation of a small amount of Ag_2MoO_4, close to the detection limit of the technique, as confirmed by PDF #72–1689. The intensity of reflections at 13.2° and 33.8° increases slightly in Ag-MoS_2 compared to bare MoS_2, which is probably due to the thicker MoS_2 film,

compared to Ag-MoS_2 (also confirmed by the RBS spectra). Such a hypothesis is also confirmed by the reverse intensity trend of the peaks coming from the FTO layer (in MoS_2 they are weaker than in Ag-MoS_2). However, upon Ag doping, there is no peak position shift, which proves that Ag doping does not significantly influence the crystal structure of MoS_2. No peak related to pure Mo oxide phases is detected in any sample, suggesting that, if present, we expect oxide phases being confined at the surface of the films.

The formation of a very small amount of Ag_2MoO_4 phase is most probably associated with the sulfur deficiency during the sputtering process. The binding energy of MoS_2 is lower than the kinetic energy of the bombarding ions. As a result, MoS_2 can be broken down to some extent into its elements during the sputtering process and recombine during transport plasma or on the substrate surface [26]. Moreover, being sulfur a lighter element than molybdenum, it can be easily re-sputtered from the substrate after having been deposited, due to high-energy neutral species bombarding the growing layer, resulting in the formation of Mo-rich nanostructure [27,28]. They might also easily be scattered by the inert gas during the target-to-substrate path. Therefore, unreacted Mo could react with Ag and forms trace of Ag_2MoO_4. No significantly intense diffraction contributions corresponding to Ag species (such as Ag or Ag_2S phases) were detected.

Fig. 3b shows the Raman spectra of MoS_2 and Ag-MoS_2 excited at 532 nm. Both samples show two characteristic bands at ~378 cm^{-1} and ~408 cm^{-1} associated with E^1_{2g} and A_{1g} vibration modes of MoS_2, respectively. The number of layers in 2D MoS_2 can be determined by the peak separation between E^1_{2g} and A_{1g} vibration modes [29]. Several studies have demonstrated that the frequency shift between the E^1_{2g} and A_{1g} bands of MoS_2 increases with the increasing the number of layers (ranging from 18 cm^{-1} to 30 cm^{-1}) [29–32]. In this work, MoS_2 presents a bulk structure as confirmed by a 30 cm^{-1} peak separation between the E^1_{2g} and A_{1g} vibration modes, in agreement with TEM and AFM results, which indicate an average thickness for the single flake in the range 30–60 nm (Fig. 1). No signal coming from either Ag_2MoO_4 or MoO_3 is recorded in the Raman spectra from both samples. This experimental evidence supports the hypotheses that: (i) the concentration of oxidized species is very small in the overall sample volume; (ii) oxidized species are mainly present at the surface of the layer, while they seem not to represent a major component of the bulk.

The chemical composition of the composite is further analyzed by Rutherford backscattering (RBS) shown in Fig. 3c. RBS spectra revealed the presence of Mo and S in the MoS_2 sample and Mo, S, and Ag in the Ag-MoS_2 composites, with a homogeneous in-depth distribution of all the detected elements. The clearest evidence of Ag is the increase in the yield of the high-energy signal in the channel region 550–700. The slight shift of the surface edge around channel 680–690 toward higher energies in the Ag-MoS_2 sample is an additional hint for the presence of Ag (since Ag is heavier than Mo). From the RUMP code simulations, the Mo:S atomic ratio is calculated as 1:1.5 in the MoS_2 sample, and Mo:S:Ag is equal to 1:1.5:0.14 in the Ag-MoS_2 sample. In both samples, sub-stoichiometric sulfur concentration is observed. The sputtered films result in Mo enrichment, with a clear sub-stoichiometry in S. The main

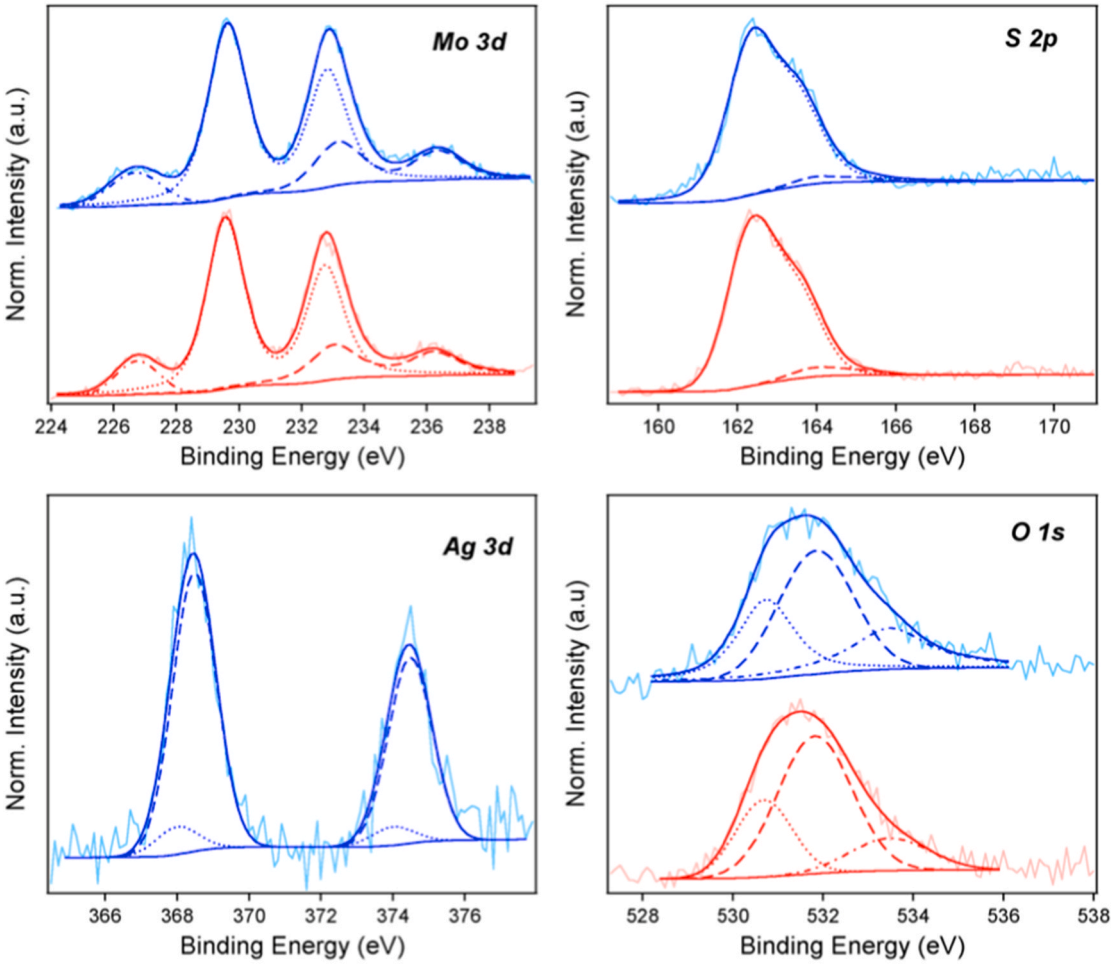

Fig. 4. XPS peaks of Mo3d, S 2p, Ag 3d, and O 1s for MoS_2 (experimental curve (light red) and deconvolution (red)) and Ag-MoS_2 (experimental curve (light blue) and deconvolution (blue)).(For interpretation of the references to colour in this figure legend, the reader is referred to the web version of this article.)

reason for this is not just the presence of residual oxygen in the sputtering chamber, but the process of preferential re-sputtering, which is induced by the bombardment from Ar neutrals during thin film growth, and which results in the enrichment of the heavier element (Mo, in the present case). We documented this process very clearly in the past in W-Si-N ternary layer, where, in that case, Si was re-sputtered resulting in a W rich film [33].

X-ray photoelectron spectroscopy (XPS) analysis was used to investigate the chemical states of the elements on the samples' surface. Fig. 4 shows the XPS peaks for the samples prepared on the nickel foam substrate. XPS peak positions (Binding Energies, eV), and atomic compositions (%) are listed in Table S1&S2. The Mo 3d core level is very similar for both MoS_2 and Ag-MoS_2 samples. Excluding the contribution at lower BE due to S 2 s (centered at 226.7 eV), the deconvolution evidences the presence of two doublets. The one at lower BEs (229.6 and 232.8 eV, for Mo $3d_{5/2}$ and $3d_{3/2,}$ respectively) is characteristic of Mo (IV) in MoS_2, while the second one at higher BEs (around 233.1 and 236.2 eV, for Mo $3d_{5/2}$ and $3d_{3/2}$, respectively) agrees with the presence of Mo(VI) in MoO_3. The atomic percentages of Mo(VI) with respect to the total amount of molybdenum are 21% and 22%, respectively, for MoS_2 and Ag-MoS_2. The presence of MoS_2 on the surface is confirmed by the position and peak shape of the S 2p peak, which is also characterized by two doublets. The main contribution at 162.5 eV is characteristic of S^{2-} in MoS_2 [9], while the small one at higher BEs (164.0 eV) can be ascribable to the presence of bridging S_2^{2-} species already observed on similar samples [34]. The presence on the surface of molybdenum(VI) oxide is confirmed by the contribution at 530.7 in O1s peak, which is characteristic of oxygen in MoO_3 [9]. Moreover, the two contributions at higher BEs (531.8 and 533.4 eV) on O 1s core level are ascribable to hydroxyl groups and adsorbed water.

Ag 3d peak core level consists of two doublets, the binding energies of the most intense (at 368.4 and 374.5 eV assigned for Ag $3d_{5/2}$ and $3d_{3/2}$, respectively), in agreement with the presence of Ag(0) [35] while the weak doublet at lower binding energies (367.9 and 373.9 eV) is ascribable to the presence of Ag(I) ions [36]. The presence of Ag(I) ions agree with XRD data, which evidences the presence of small impurities of Ag_2MoO_4. Also, the BEs (around 233.2 and 236.3 eV are in agreement with the presence of Mo(VI) in Ag_2MoO_4. The XPS quantitative analysis reveals a Mo:S atomic ratio of 1:2 for MoS_2, while a Mo:S:Ag atomic ratio equal to 1:2:0.13 is measured for Ag-MoS_2. These values indicate a variation in composition between the bulk of the material (where Mo: S = 1:1.5, as pointed out by the RBS) and the surface. The deposition rate during the sputtering process is about 0.5 nm/s (see Experimental section). The formation of a surface layer, few nanometers thick, in which the composition is mainly determined by the residual atmosphere, once the plasma source is turned off or a shutter covers the substrate, is compatible with the technical features of magnetron sputtering deposition, and can explain the discrepancy between RBS and XPS.

An important observation relies with the presence of oxides at the surface of both the samples. While the presence of oxidized species can be regarded as an impurity, such presence confirms a general trend in MoS_2-based materials, for which oxidized species are ubiquitously found in XPS analysis at the surface of various layers [37–44]. Our results are also in agreement with Raman analyses from other studies, which do not record the presence of oxidized Mo, even in presence of a clear signal related to MoO_3 in XPS spectra [37–44]. These experimental findings testify that MoO_3 (and, in this case, also Ag_2MoO_4) are typically present at the surface of MoS_2-based compounds, and it is rather difficult, if not impossible, producing an oxygen-free surface. Such impurities may of course participate in the catalytic processes. However, in the present case, we can see that the main parameter influencing the catalytic properties is the presence of Ag(0), as detected by XPS, which induces a substantial boost of the catalytic activities in the Ag-containing sample.

3.2. Functional characterization

To assess the electrocatalysis for the forward process, namely OER, the linear sweep voltammetry (LSV) was carried out in an alkaline aqueous electrolyte and displayed in Fig. 5a-f. The concentration effect of Ag on the catalyst performance is first conducted and results are discussed in ESI and Fig. S9. For the optimized sample (Fig. 5a), the nickel surface undergoes well-defined electrochemical oxidation in aqueous alkaline media. The position of anodic peak current associated with nickel single-electron oxidation (1.38 V vs RHE, Fig. 5(a)) is considered as inherent standard potential. In nickel-based electrocatalyst, the overpotentials needed to achieve a certain OER current density are reported above the Ni^{2+}/Ni^{3+} redox potential [45–47]. Both MoS_2 and $AgMoS_2$ modified NF electrodes show a substantial increase of the current density at the positive polarizations from $Ni^{2+}/Ni3^{+}$ redox potential, which are associated with the onset of the OER. The surface modification of NF led to the mitigation of the kinetic loss of the electrode process visible as the decrease of overpotential needed to reach a current density of 100 mA/cm^2 (Fig. 5a). Ag-MoS_2 catalyst needs an overpotential of 370 mV, while MoS_2 needs 500 mV to produce a current density of 100 mA/cm^2. The presence of silver reduces overpotential further by 130 mV, demonstrating the electrocatalytic phenomena behind the doping of MoS_2 by silver.

The lowering of the Tafel slope from 86 mV dec^{-1} to 58.6 mV dec^{-1} (Fig. 5b) due to the presence of the silver, illustrating the change of the rate-determining step of the whole electrode reaction and higher currents in the kinetic control region of applied potentials.

The Tafel slope lower than 120 mV dec^{-1} proves the incomplete surface coverage with intermediates converted in a subsequent rate-determining step [48]. In other words, the decrease of the Tafel slope for OER observed in our study implies the existence of interim steps between the formation of the dominating adsorbate and the rate-determining step. The presence of silver favors the thermodynamics of hydroxyl radical ($OH^{\bullet}$) adsorption on the composite (being the radicals adsorbed on Ag itself) [49], which might be the reason for the lowering of the Tafel slope and the observed electrocatalytic phenomena.

Similar Tafel slopes were obtained for transition metal hydroxides, which are among the most efficient OER catalysts [50–52] indicating that the as-synthesized Ag-MoS_2 is a superior electrocatalyst towards OER. The change of the reaction mechanism by the integration of silver induces an improvement in the operational stability of the electrocatalyst (Fig. 5c and ESI Fig. S10). Indeed, Ag-MoS_2- and MoS_2-modified electrode shows more than 80% and 67% retentions of the OER current density during 22 h of continuous operation at 1.55 V vs RHE (Fig. 5c and Fig. S10 a), respectively. Coherently, the absence of the degradation of Ag-MoS_2 was supported by the voltammetry data acquired after the operational stability test (Inset in Fig. 5c) in comparison with pristine MoS_2 (Fig. S10).

A possible method to measure the specific surface of our electrode is BET. While the standard porosimetry and gas adsorption methods lack sensitivity for characterization of thin metallic films. Therefore we have used electrochemical methods for the determination of the surface area of thin films of interconnected nickel foam. The integration of silver leads to more than a 30% increase of capacitive currents and more than a 13% increase in the film capacitance. This effect might be due to both the contribution of a metallic moiety of the high capacitance of the electric double layer in the semiconducting MoS_2 and the morphology change leading to the increase of the electrochemically active surface area (ECSA). To grasp the roughness effect on the rates of OER [53], the values of charge transfer resistance normalized either on voltammetric electrocapacitive currents (Fig. 5d,e, and Fig. S11) or double-layer capacitance values estimated by the fitting of impedance data have been compared. Ag-MoS_2 shows more than 1.5 times an increase in the roughness-normalized rate of OER compared to MoS_2 illustrating the effect of the reaction mechanism alteration by silver doping.

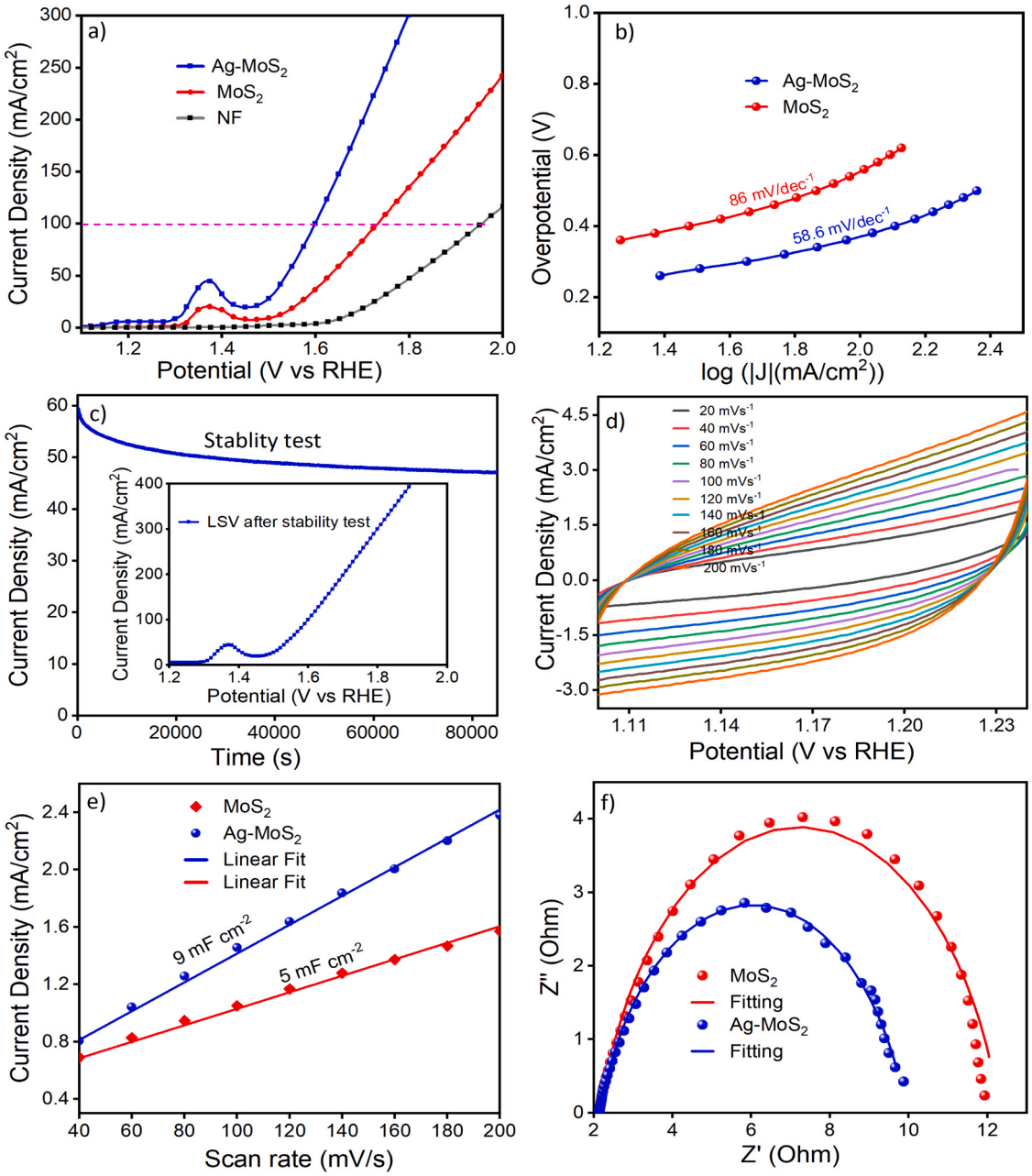

Fig. 5. The OER performance of the as-prepared catalyst. (a) Polarization curves of Ag-MoS_2, MoS_2, and Nickel foam (NF) after iR compensation. (b) Corresponding Tafel plots are derived from the polarization curves of the catalysts (Ag-MoS_2 and MoS_2). (c) Chronoamperometry measurement for Ag-MoS_2 stability test with the inset showing the LSV after the stability test. (d, e, f) Cyclic voltammetry, double-layer capacitance, and impedance measurement for Ag-MoS_2 and MoS_2.

The electrochemical impedance spectroscopy (EIS) was utilized to quantify both kinetic and electrocapacitive phenomena of electrocatalysts at the applied potential of kinetic control (1.5 V) (Fig. 5f). The analysis of impedance spectra was carried out by fitting with simplified Randles cell as an equivalent circuit (Fig. S12), comprising the solution resistance R_1 used for iR compensation during voltammetry measurements in series with an RC unit of film capacitance and the charge transfer resistance. Since the interfaces of porous films are not ideally smooth, an impedance analysis required a distributed circuit model featuring constant phase elements (CPE) rather than pure capacitors. The capacitance values have been calculated as [54]:

$$C = \left(Q(R_1)^{(1-a)}\right)^{1/a} \quad (1)$$

where R_1 is the solution resistance, Q is a fitting parameter of the CPE and α is the fitting exponent factor, which varies from 0 to 1. When α is approaching 0, the CPE behaves as a pure resistor, and when $\alpha = 1$ the CPE represents a pure capacitor. A single set of parameters (Fig. S12, and Table S3) has been used to instantaneously fit the real and imaginary parts of the impedance over the frequency range from 0.25 Hz to 4 kHz. A value of the fitting quality parameter $\chi^2 \leq 0.001$ obtained for all spectra indicates a very good fit. The presence of silver leads to more than a 20% decrease of the R_{CT} manifesting the increase of the overall rate of the electrode reaction.

The apparent exchange current density ($J_0{*}n$), representing the driving force-free rate of the process, is calculated up to a constant as:

$$J_0{*}n = (R{*}T)/(F{*}R_{CT}{*}A) \quad (2)$$

Where R_{CT} is the charge transfer resistance (Ω), R is the gas constant

(8.31 J mol^{-1} K^{-1}), T is the temperature (298 K), A is the geometrical area of the electrode (1 cm^2), F is the Faraday's constant (96,485 A s mol^{-1}) and n is the number of electrons. The presence of silver results in the apparent exchange current density of 3.3 mA/cm^2, while the pristine MoS_2 shows more than 20% lower value (2.5 mA/cm^2).

Due to its moderate electronegativity, Ag can promote molybdenum to a higher oxidation state for maintaining charge balance. Therefore, molybdenum stays at a higher valence state and becomes an active site center for the OER process due to the increase of its oxidation state. Also, the presence of Mo(VI) can help to draw Ag 3d electrons and further oxidized it to a higher oxidation state due to its relatively higher electronegativity [55]. As a result, Ag can attract OER intermediate (such as OH) and facilitates the OER process. Overall, the improved catalytic activity of the composite is associated with the presence of high-valent Mo, and low oxidation state Ag, which helps in tuning the electronic structure of the composites. The strong mutual interaction between Ag and Mo as well as the favorable interaction of the OH intermediates with Ag surfaces results in an overall synergistic effect, which improves the overall OER process. Furthermore, the substrate (NF) and the subsequent annealing improves the catalyst stability and provides favorable morphology with a large surface area, high porosity, and uniform distribution of catalyst particles. The characteristics of OER activity on Ag-MoS_2 are compared with published reports (Table S4). Notably, Ag-MoS_2 outperforms most of the reported OER electrocatalysts in terms of onset potential and overpotential, suggesting the presence of silver improves the performance of the electrocatalyst.

The oxygen reduction reaction (ORR) activity of both catalysts was evaluated using a rotating disk electrode (RDE) and rotating ring disk electrode (RRDE) methods. The ORR measurement is performed only for the optimized catalyst. The polarization curve of Ag-MoS_2 recorded at different electrode rotation rate is closer to the sigmoidal shape compared to MoS_2 (Fig. 6a,b). As displayed in the LSV, the region between 0.9 and 0.85 V vs RHE, for which the current densities are independent of the rotating rate, indicates a purely kinetic controlled region, resulting in kinetic current density (j_k). While the region (0.6–0.45 vs RHE) is limited by diffusion of O_2 and the corresponding current is a diffusion-controlled current density (J_d). The slow kinetics at the electrode surface can be evidenced by the slope of the Levich plot (limiting current density against $\omega^{1/2}$) (Fig. S13a,b, and Table S5). The slope intercepts the vertical axis above zero and falls off gradually with the increase of the rotational rate of the RDE for values measured in between 0.4 and 0.60 V vs RHE, indicating the slow electron transfer kinetics. However, comparing both catalysts, it is evident that the presence of silver improves the ORR activity by facilitating the electron transfer kinetics near the electrode surface. To verify the total electron transfer number (n) per O_2 molecule and the kinetic current density (j_k), the Koutecky–Levich (K-L) analysis was performed and the result is displayed in Fig. 6b, d (details and methods are given in ESI part, the slopes and intercepts are listed in Table S6).

Oxygen can be directly converted into water or hydroxide by a direct 4-electron reduction pathway or it can be converted to HO_2^- via a 2-

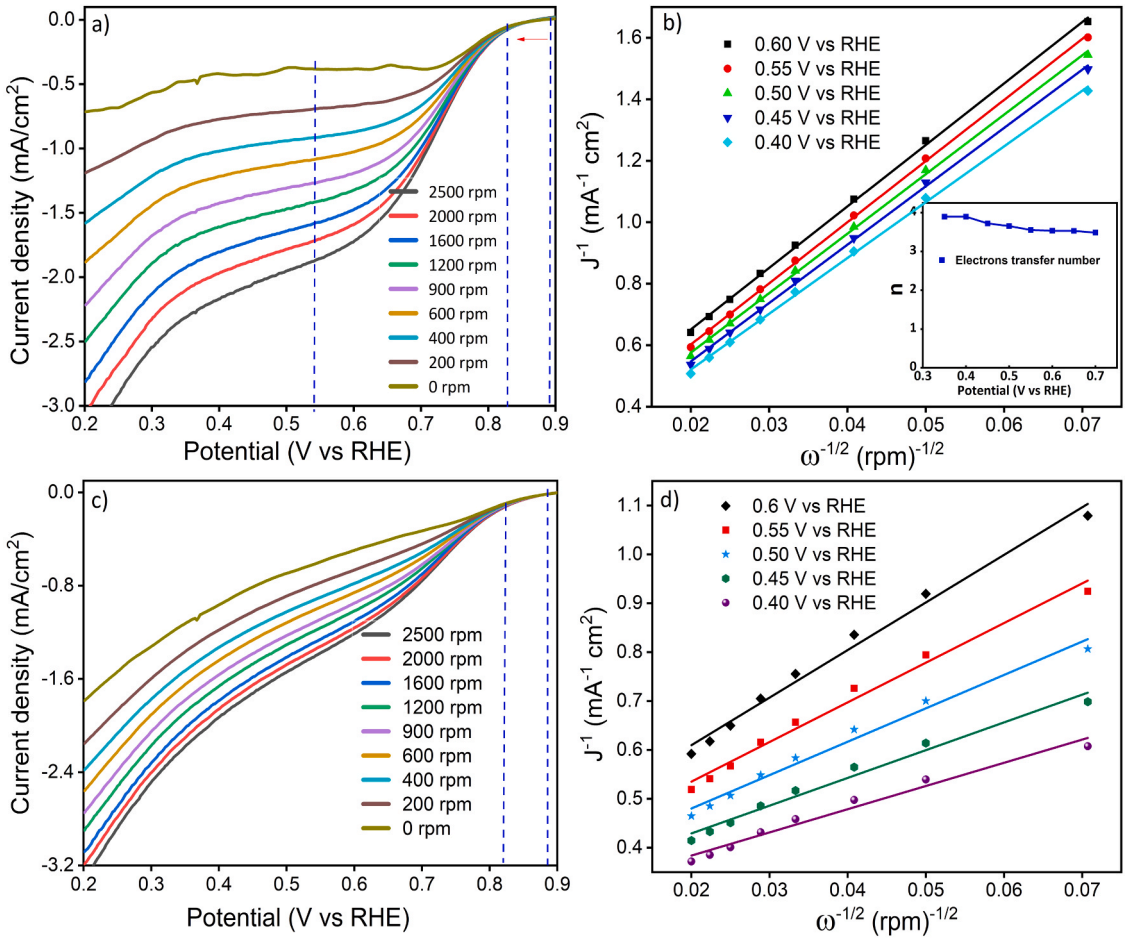

Fig. 6. Rotating-disk voltammograms of the nanocomposites in O_2 saturated 0.1 M KOH at room temperature with a sweep rate of 20 mV s^{-1} at different rotating rates from 0 to 2500 rpm for Ag-MoS_2 (a) and MoS_2 (c). Corresponding Koutecky–Levich plots of J^{-1} vs. $\omega^{-1/2}$ at 0.4, 0.45, 0.5, 0.55, and 0.60 V vs. RHE and associated linear fit for calculating the electron number AgMoS_2 and MoS_2 (b, d). The inset in (b) is the electron transfer numbers at the different potentials for Ag-MoS_2.

electron reduction pathway [56]. The values of n and J_k are obtained from the slope and intercept of the K-L plots, respectively. An average slope (B = 19.5 mA^{-1} cm^2 $rpm^{1/2}$) is obtained for Ag-MoS_2 within the potential range 0.7–0.40 V vs RHE. The calculated slope is independent of the applied potential for all K-L plots obtained within that potential range, suggesting a similar electron transfer number (n). The total electron transfer number calculated within the potential range (0.75–0.35 V vs RHE) varies from 2 to 4 (inset of Fig. 6b). The electron transfer number values are given in ESI Table S4. The K-L analysis of MoS_2 results in potential dependent intercept and slope, which result in a different n value in the mentioned potential range. The result from the K-L analysis suggests a total of 4 electron reduction mechanism of O_2 molecule on the Ag-MoS_2 catalyst surface, in agreement with the result obtained for $AgMoS_2$ hybrid [57], with Pt-based ORR catalyst stated elsewhere [56,58,59], suggesting that Ag-MoS_2 have a possibility of replacing nobel metal electrocatalyst.

For further in-situ detection of reaction intermediates and identify the reaction pathway, we utilized an RRDE equipped with an independent platinum ring electrode. The LSV using RRDE is displayed in Fig. S14 a, b. By modulating the electrode rotation speed, we defined the regions of both rotation-dependent and independent currents corresponding to diffusion and kinetic controls, respectively. The integration of silver does not change the rate-determining step of the ORR, which is illustrated with a minor change of the Tafel slopes estimated from the background-subtracted currents in the kinetic control region (Fig. 7a, b, and ESI Table S7; ca. 46 mV dec^{-1} and ca. 30 mV dec^{-1} for pristine and silver-doped MoS_2, respectively). This suggests a mechanism of ORR on the pristine and silver-decorated MoS_2 as EEC*, (i.e. the two consecutive single electron transfers followed by the chemical step as rate-determining) [60]. Decisively, the net ORR currents are still higher on Ag-MoS_2 in hydrodynamic conditions (Fig. S15). Indeed, the background-subtracted currents on Ag-MoS_2 are two times higher at 0.65 V (vs RHE). This illustrates the co-catalysis of ORR on Ag-MoS_2.

Fig. 7c,d shows the total number of electron transfer (n) and the percentage of HO_2^- generated during the ORR as a function of potential using RRDE techniques (See ESI for the calculations of n and % HO_2^-). At a large overpotential of 0.2 V, the values of n for Ag-MoS_2 are 3.2 (at ω = 900 rpm), which decreases to a minimum of 2.7 at lower potential (0.6 V). For the same rotational rate, the % HO_2^- yield remains at around 50% at 0.2 V and 70% at 0.6 V. However, for MoS_2, the electron transfer number remains nearly constant through the given potential range compared to Ag-MoS_2 and resulting in a lower percentage of peroxide yield.

The linearity of the plot NI_d/I_r is a reliable criterion for the branched reaction pathways of the ORR mechanism as shown in Fig. S16. Using the two important plots $\frac{I_d}{I_r}$ and $\frac{I_{dl}}{I_{dl}-I_d}$ *vs* $\omega^{-1/2}$ (Fig. S16 and Fig. S17), the rate constants were determined and listed in Table S8 (see ESI for details on calculations).

To get insight into the ORR reaction pathway, the reaction scheme proposed by Damjanovic et al. [61] and other related works [62,63] were employed and finally, the reaction pathways of the catalyst were suggested as described in Fig. 8. Based on the rate constants calculations, there is an obvious change in the reaction mechanism upon changing potential. As a result, the calculated rate constant is potential dependent. The ORR on MoS_2 and Ag-MoS_2 in alkaline media proceeds through a mixed 4e direct path (Eq. 4) and a 2 + 2 serial route (Eqs. 5,6). The direct path to hydroxide can be described as:

$$O_2 + 4H_2O + 4e^- \rightarrow 2H_2O + 4OH^- \quad (4)$$

The serial route can be described by (Eq. 5), for which the ionized hydrogen peroxide is formed as a mobile intermediate:

$$O_2 + H_2O + 2e^- \rightarrow HO_2^- + OH^- \quad (5)$$

The latter is converted further by means of hydrogen peroxide

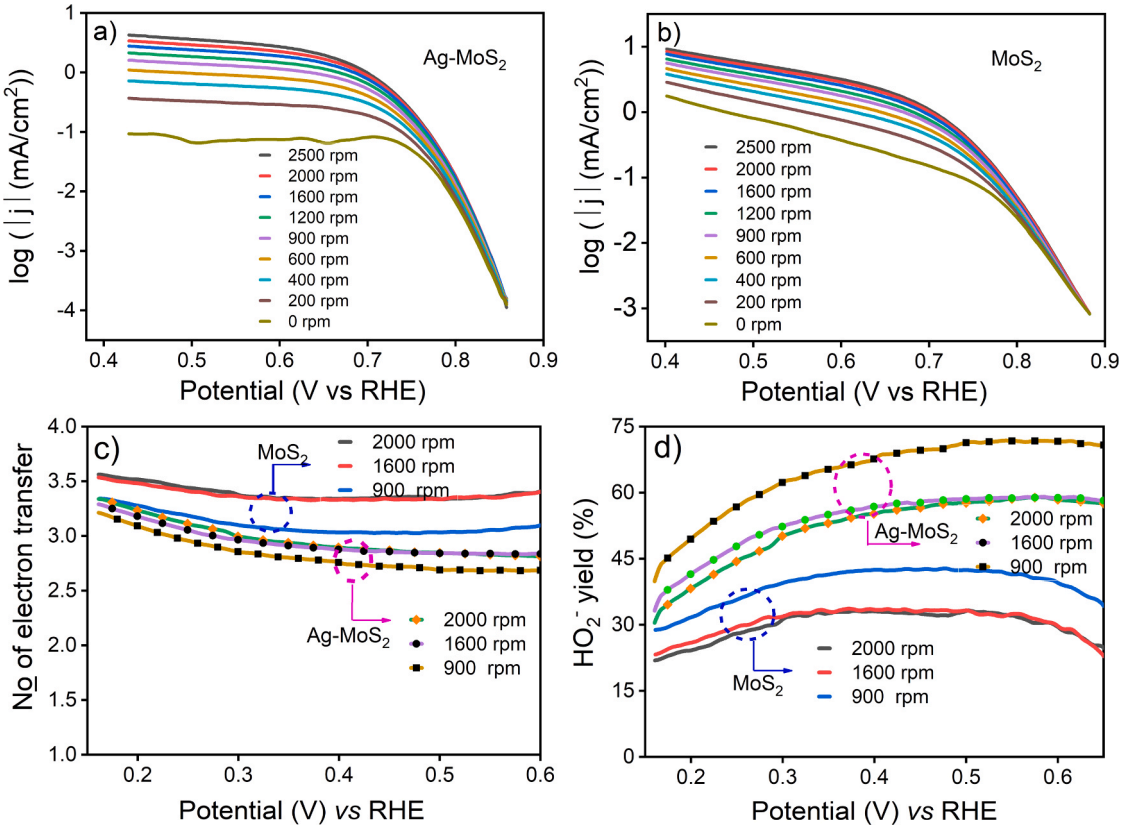

Fig. 7. a, b) Tafel slope obtained from the net current density of the RDE after mass transport correction at different rotational rates. c, d) calculated electron transfer number (n), and %HO_2^- yield at a selected rotational rate for Ag-MoS_2 and MoS_2.

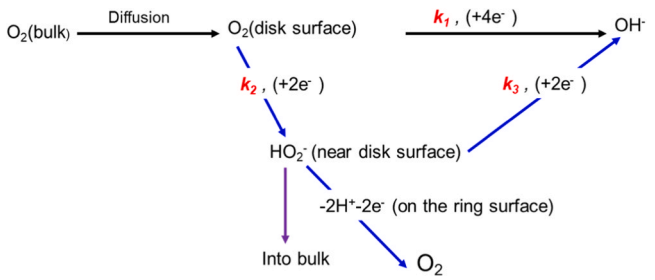

Fig. 8. Schematic representation of the proposed reaction mechanism pathways for the as-synthesized catalysts.

reduction reaction (HPRR):

$$HO_2^- + H_2O + 2e^- \rightarrow 3OH^- \quad (6)$$

For MoS_2, the rate constant k_1 is larger than k_2, suggesting that there are 4 electron pathways, for which O_2 can be converted into OH^- on the MoS_2 surface (see Fig. 8). Therefore, the pristine MoS_2 catalyzes the O_2 molecule mainly via the reaction path described by Eq. (4) evidenced by higher k_1 values.

The small difference in the ratio of the rate constants (k_1 to k_2) suggests that a sequential two-electron reduction or a two-electron reduction with subsequent HO_2^- decomposition cannot be excluded (Table S8, Fig. 8). Also, the deviation of the number of transferred electrons per oxygen molecule from four and the visible current of peroxide detection on the ring electrode manifest the presence of hydrogen peroxide available for further electrochemical reduction to OH^- via HPRR (6) or for the desorption followed by convective transport towards the detection on the ring electrode. The presence of silver changes the reaction pathway as evidenced by larger k_2 values compared to k_1 as shown in Table S8. Due to silver the ORR on Ag-MoS_2 mainly proceeds via a 2 + 2 serial route for which the hydrogen peroxide is formed as a mobile intermediate and later converted to OH^- (reaction path (5) and (6)). There is also a trace amount of O_2 reduced to OH^-via the 4e transfer reaction pathway, which could suggest the presence of active sites on the surface which differ from the ones on bare MoS_2.

The intermediate peroxide might also disproportionate to oxygen and hydroxide. Importantly, the enhancement of product diffusion from the electrode surface suppresses the disproportionation [64], yielding the increase of peroxide leakage in the bulk.

In a full coherency, the integration of silver in MoS_2 leads to the decrease of the number of transferred electrons (Fig. 7c) due to the interplay of 2 + 2 electron reduction with the additional 2-electron process. The increase of the peroxide yield observed on Ag-MoS_2 (Fig. 7d) manifests the convective removal of 2-electron ORR product bypassing disproportionation (5). Comparing the k_3 values of Ag-MoS_2 and MoS_2 there is 2.5–6 times faster conversion efficiency due to the presence of silver. This evidence supports that silver is an effective cocatalyst, which speeds up the reduction of the peroxide to OH^- much faster than bare MoS_2.

Furthermore, the disproportionation and the backward reaction of the intermediates (peroxide) to oxygen and hydroxide were evaluated using the scheme proposed by Bagotskii et al. [65] shown in Fig. S18. However, the rate constants result in negative values, similar to other's work [66] which is due to the very small values of the backward rate constant k_4.

Generally, hydrogen peroxide as an intermediate ORR product on silver can be reduced further on MoS_2 by HPRR (6) yielding an additional contribution to the efficiency of the chemical-to-electrical energy conversion. For both catalysts, an alternative sequential 2 + 2 or a direct 4 electron reduction pathway, as well as a two-electron reduction with subsequent HO_2^- disproportionation is an additional possible mechanism of ORR path on pristine and silver doped MoS_2.

4. Conclusion

In this study, we synthesized silver-decorated nanoflakes of MoS_2 (Ag-MoS_2) by magnetron co-sputtering and investigated their performance towards OER and ORR activity. The morphological characterization confirms that MoS_2 nanoflakes grow vertically with a uniform distribution, and silver is homogeneously distributed on the MoS_2 surface. The resulting Ag-MoS_2 composite is characterized by efficient surface-active sites and a considerably higher catalytic performance compared to bare MoS_2, outperforming some of the most efficient catalysts reported to date.

The highest catalytic activity of the Ag-MoS_2 composite is evidenced by the very low Tafel slope (58.6 mV dec^{-1}), which suggests favorable OH^- adsorption with subsequent deprotonation step as a rate-determining step. The as-synthesized Ag-MoS_2 shows a very low charge transfer resistance (7.4 Ω), a relatively higher double layer capacitor (9 mF cm^{-2}), and possesses extended long-term durability for 22 hrs., by producing 50 mA/cm^2 at a potential of 1.55 V. The best performance of the composite is associated with the presence of silver, which has an important role in modulating the high-valent Mo oxidation state, which increases the active reaction sites for OER intermediate.

RDE and RRDE analysis show that the as-synthesized catalyst possesses a slope of 28 mV $decade^{-1}$ (for Ag-MoS_2) and 49 mV $decade^{-1}$ (for MoS_2) at 2500 rpm. Moreover, the Ag-MoS_2 catalyst follows a mixed 2 + 2 and 4 electron pathways, suggesting that the O_2 molecule reduces directly into HO_2^- within the diffusion-limited region. A high HO_2^- percentage yield is observed for Ag-MoS_2 compared to MoS_2 within the diffusion-limited potential region. The hydrogen peroxide product on silver can be further reduced on the MoS_2 surface, which contributes to the additional efficiency of the chemical-to-electrical energy conversion. There is a 2.5–6 times faster conversion rate of the HO_2^- to OH^- due to the presence of silver for Ag-MoS_2, which supports the claim that silver is an effective cocatalyst, which speeds up the reduction of the intermediate peroxide much faster than bare MoS_2.

These results offer an insight into OER and ORR activity of the composite (Ag-MoS_2), which can serve as an efficient bifunctional catalyst. This method of surface engineering using magnetron co-sputtering demonstrated effective in developing highly efficient and novel catalysts capable of working for both OER and ORR.

CRediT authorship contribution statement

Getachew Solomon: Conceptualization, Investigation, Methodology, Data curation, Writing - original draft preparation. **Mojtaba Gilzad Kohan:** Data curation, Investigation. **Mikhail Vagin:** Investigation, Data curation, **Federica Rigoni:** Methodology, Data curation. **Raffaello Mazzaro:** Methodology, Data curation. **Marta Maria Natile:** Methodology, Data curation. **Shujie You:** Investigation, Data curation. **Vittorio Morandi:** Supervision, Data curation, **Isabella Concina:** Supervision, Data curation. **Alberto Vomiero:** Supervision, Validation, Data curation, Writing - review & editing.

Declaration of Competing Interest

The authors declare no conflict of interest or personal relationships that could have appeared to influence the work reported in this paper.

Acknowledgments

The authors acknowledge the financial support from Knut & Alice Wallenberg foundation, Sweden, the Swedish foundation consolidator fellowship, Sweden, the European Union's Horizon 2020 research and innovation program under grant agreement No 654002, Luleå University of Technology laboratory fund program, Sweden, and Kempe Foundation for partial funding, Sweden. I.C. acknowledges VINNOVA under the VINNMER Marie cure incoming Grant for partial funding

(project “Light Energy”, LiEN, 2015-01513), Sweden.

M.V. would like to acknowledge the Swedish Research Council (VR 2019-05577, Flexible metal-air primary batteries), Sweden. M.M.N. acknowledges the MIUR-PON TARANTO (ARS01_00637) for partial funding, Italy. R.M. and V.M. acknowledge the European Union’s Horizon 2020 research and innovation program under Graphene Core2 785219 – Graphene Flagship for partial funding.

Appendix A. Supporting information

Supplementary data associated with this article can be found in the online version at doi:10.1016/j.nanoen.2020.105664.

References

[1] G. Solomon, M.G. Kohan, A. Landström, A. Vomiero, I. Concina, Semiconducting metal oxides empowered by graphene and its derivatives: progresses and critical perspective on selected functional applications, J. Appl. Phys. 128 (2020), 180905.
[2] H. Tan, J. Tang, J. Kim, Y.V. Kaneti, Y.M. Kang, Y. Sugahara, Y. Yamauchi, Rational design and construction of nanoporous iron- and nitrogen-doped carbon electrocatalysts for oxygen reduction reaction, J. Mater. Chem. A. 7 (2019) 1380–1393.
[3] X. Li, B.Y. Guan, S. Gao, X.W. Lou, A general dual-templating approach to biomass-derived hierarchically porous heteroatom-doped carbon materials for enhanced electrocatalytic oxygen reduction, Energy Environ. Sci. 12 (2019) 648–655.
[4] P. Mani, R. Srivastava, P. Strasser, Dealloyed Pt-Cu core-shell nanoparticle electrocatalysts for use in PEM fuel cell cathodes, J. Phys. Chem. C. 112 (2008) 2770–2778.
[5] J. Wang, H.X. Zhong, Z.L. Wang, F.L. Meng, X.B. Zhang, Integrated three-dimensional carbon paper/carbon tubes/cobalt-sulfide sheets as an efficient electrode for overall water splitting, ACS Nano 10 (2016) 2342–2348.
[6] M. Ledendecker, S. Krick Calderón, C. Papp, H.-P. Steinrück, M. Antonietti, M. Shalom, The synthesis of nanostructured Ni 5 P 4 films and their use as a non-noble bifunctional electrocatalyst for full water splitting, Angew. Chem. 127 (2015) 12538–12542.
[7] G. Solomon, R. Mazzaro, V. Morandi, I. Concina, A. Vomiero, Microwave-assisted vs. conventional hydrothermal synthesis of mos2 nanosheets: application towards hydrogen evolution reaction, Crystals 10 (2020) 1–12.
[8] B. Tang, Z.G. Yu, H.L. Seng, N. Zhang, X. Liu, Y.W. Zhang, W. Yang, H. Gong, Simultaneous edge and electronic control of MoS2 nanosheets through Fe doping for an efficient oxygen evolution reaction, Nanoscale 10 (2018) 20113–20119.
[9] G. Solomon, R. Mazzaro, S. You, M.M. Natile, V. Morandi, I. Concina, A. Vomiero, Ag 2 S/MoS 2 nanocomposites anchored on reduced graphene oxide: fast interfacial charge transfer for hydrogen evolution reaction, ACS Appl. Mater. Interfaces 11 (2019) 22380–22389.
[10] M. Wang, P. Ju, W. Li, Y. Zhao, X. Han, Ag2S nanoparticle-decorated MoS2 for enhanced electrocatalytic and photoelectrocatalytic activity in water splitting, Dalt. Trans. 46 (2017) 483–490.
[11] J. Mao, P. Liu, C. Du, D. Liang, J. Yan, W. Song, Tailoring 2D MoS2 heterointerfaces for promising oxygen reduction reaction electrocatalysis, J. Mater. Chem. A 7 (2019) 8785–8789.
[12] S.J. Rowley-Neale, G.C. Smith, C.E. Banks, Mass-producible 2D-MoS2-impregnated screen-printed electrodes that demonstrate efficient electrocatalysis toward the oxygen reduction reaction, ACS Appl. Mater. Interfaces 9 (2017) 22539–22548.
[13] Y. Zhang, T. Han, J. Fang, P. Xu, X. Li, J. Xu, C.C. Liu, Integrated Pt2Ni alloy@Pt core-shell nanoarchitectures with high electrocatalytic activity for oxygen reduction reaction, J. Mater. Chem. A 2 (2014) 11400–11407.
[14] H. Erikson, A. Sarapuu, K. Tammeveski, Oxygen reduction reaction on silver catalysts in alkaline media: a minireview, ChemElectroChem 6 (2019) 73–86.
[15] A. Qaseem, F. Chen, X. Wu, R.L. Johnston, Pt-free silver nanoalloy electrocatalysts for oxygen reduction reaction in alkaline media, Catal. Sci. Technol. 6 (2016) 3317–3340.
[16] K.L. Yan, J.Q. Chi, Z.Z. Liu, B. Dong, S.S. Lu, X. Shang, W.K. Gao, Y.M. Chai, C. G. Liu, Coupling Ag-doping and rich oxygen vacancies in mesoporous NiCoO nanorods supported on nickel foam for highly efficient oxygen evolution, Inorg. Chem. Front. 4 (2017) 1783–1790.
[17] Y. Zhou, Q. Lu, Z. Zhuang, G.S. Hutchings, S. Kattel, Y. Yan, J.G. Chen, J.Q. Xiao, F. Jiao, Oxygen reduction at very low overpotential on nanoporous Ag catalysts, Adv. Energy Mater. 5 (2015), 1500149.
[18] P. Singh, D.A. Buttry, Comparison of oxygen reduction reaction at silver nanoparticles and polycrystalline silver electrodes in alkaline solution, J. Phys. Chem. C 116 (2012) 10656–10663.
[19] X. Li, G. Zhu, L. Xiao, Y. Liu, Z. Ji, X. Shen, L. Kong, S.A. Shah, Loading of Ag on Fe-Co-S/N-doped carbon nanocomposite to achieve improved electrocatalytic activity for oxygen evolution reaction, J. Alloy. Compd. 773 (2019) 40–49.
[20] C. Lee, K. Shin, C. Jung, P.P. Choi, G. Henkelman, H.M. Lee, Atomically embedded ag via electrodiffusion boosts oxygen evolution of coooh nanosheet arrays, ACS Catal. 10 (2020) 562–569.
[21] C. Tang, H. Sen Wang, H.F. Wang, Q. Zhang, G.L. Tian, J.Q. Nie, F. Wei, Spatially confined hybridization of nanometer-sized NiFe hydroxides into nitrogen-doped graphene frameworks leading to superior oxygen evolution reactivity, Adv. Mater. 27 (2015) 4516–4522.
[22] D.K. Bediako, Y. Surendranath, D.G. Nocera, Mechanistic studies of the oxygen evolution reaction mediated by a nickel-borate thin film electrocatalyst, J. Am. Chem. Soc. 135 (2013) 3662–3674.
[23] D.A. Shirley, High-resolution x-ray photoemission spectrum of the valence bands of gold, Phys. Rev. B. 5 (1972) 4709–4714.
[24] J.F. Moulder, W.F. Stickle, P.E. Sobol, K.D. Bomben, Handbook of X-ray photoelectron spectroscopy: a reference book of standard spectra for identification and interpretation of XPS data, 1992.
[25] F. Shi, J. He, B. Zhang, J. Peng, Y. Ma, W. Chen, F. Li, Y. Qin, Y. Liu, W. Shang, P. Tao, C. Song, T. Deng, X. Qian, J. Ye, J. Wu, Plasmonic-enhanced oxygen reduction reaction of silver/graphene electrocatalysts, Nano Lett. 19 (2019) 1371–1378.
[26] B.C. Stupp, Synergistic effects of metals co-sputtered with MoS2, Thin Solid Films 84 (1981) 257–266.
[27] A. Vomiero, E.B. Marchi, G. Mariotto, A. Quaranta, G. Della Mea, G. Ottaviani, R. Tonini, M. Butturi, G. Martinelli, Composition and resistivity changes of reactively sputtered W-Si-N thin films under vacuum annealing, Appl. Phys. Lett. 88 (2006) 1–3.
[28] A. Vomiero, E.B. Marchi, G. Mariotto, G. Della Mea, A. Scandurra, O. Puglisi, The role of N in the resputtering inhibition of Si in W-Si-N reactively sputtered thin layer, J. Appl. Phys. 97 (2005), 034905.
[29] H. Li, Q. Zhang, C.C.R. Yap, B.K. Tay, T.H.T. Edwin, A. Olivier, D. Baillargeat, From bulk to monolayer MoS 2: evolution of Raman scattering, Adv. Funct. Mater. 22 (2012) 1385–1390.
[30] G. Plechinger, S. Heydrich, J. Eroms, D. Weiss, C. Schüller, T. Korn, Raman spectroscopy of the interlayer shear mode in few-layer MoS 2 flakes, Appl. Phys. Lett. 101 (2012), 101906.
[31] M.A. Nikpay, S.Z. Mortazavi, A. Reyhani, S.M. Elahi, Sputtered MoS2layer as a promoter in the growth of MoS2nanoflakes by TCVD, Mater. Res. Express 5 (2018), 015032.
[32] E. Er, H.L. Hou, A. Criado, J. Langer, M. Möller, N. Erk, L.M. Liz-Marzán, M. Prato, High-Yield preparation of exfoliated 1T-MoS2 with SERS activity, Chem. Mater. 31 (2019) 5725–5734.
[33] A. Vomiero, S. Frabboni, E.B. Marchi, A. Quaranta, G. Della Mea, G. Mariotto, L. Felisari, Structural and functional characterization of W-Si-N sputtered thin films for copper metallizations, MRS Proc. 812 (2004) F3.10.
[34] A. Tahira, Z.H. Ibupoto, R. Mazzaro, S. You, V. Morandi, M.M. Natile, M. Vagin, A. Vomiero, Advanced electrocatalysts for hydrogen evolution reaction based on core-shell MoS2/TiO2 nanostructures in acidic and alkaline media, ACS Appl. Energy Mater. 2 (2019) 2053–2062.
[35] J.R. Ansari, N. Singh, S. Mohapatra, R. Ahmad, N.R. Saha, D. Chattopadhyay, M. Mukherjee, A. Datta, Enhanced near infrared luminescence in Ag@Ag 2 S core-shell nanoparticles, Appl. Surf. Sci. 463 (2019) 573–580.
[36] D. Xu, B. Cheng, J. Zhang, W. Wang, J. Yu, W. Ho, Photocatalytic activity of Ag 2 MO 4 (M = Cr, Mo, W) photocatalysts, J. Mater. Chem. A. 3 (2015) 20153–20166.
[37] L. Guo, Z. Yang, K. Marcus, Z. Li, B. Luo, L. Zhou, X. Wang, Y. Du, Y. Yang, MoS2/TiO2 heterostructures as nonmetal plasmonic photocatalysts for highly efficient hydrogen evolution, Energy Environ. Sci. 11 (2018) 106–114.
[38] H. Lin, L. Yang, X. Jiang, G. Li, T. Zhang, Q. Yao, G.W. Zheng, J.Y. Lee, Electrocatalysis of polysulfide conversion by sulfur-deficient MoS 2 nanoflakes for lithium–sulfur batteries, Energy Environ. Sci. 10 (2017) 1476–1486.
[39] J. Hu, B. Huang, C. Zhang, Z. Wang, Y. An, D. Zhou, H. Lin, M.K.H. Leung, S. Yang, Engineering stepped edge surface structures of MoS2 sheet stacks to accelerate the hydrogen evolution reaction, Energy Environ. Sci. 10 (2017) 593–603.
[40] I.S. Amiinu, Z. Pu, X. Liu, K.A. Owusu, H.G.R. Monestel, F.O. Boakye, H. Zhang, S. Mu, Multifunctional Mo-N/C@MoS 2 electrocatalysts for HER, OER, ORR, and Zn-Air Batteries, Adv. Funct. Mater. 27 (2017), 1702300.
[41] S. Guo, X. Li, X. Ren, L. Yang, J. Zhu, B. Wei, Optical and electrical enhancement of hydrogen evolution by MoS2@MoO3 core–shell nanowires with designed tunable plasmon resonance, Adv. Funct. Mater. 28 (2018), 1802567.
[42] Y. Huang, Y. Sun, X. Zheng, T. Aoki, B. Pattengale, J. Huang, X. He, W. Bian, S. Younan, N. Williams, J. Hu, J. Ge, N. Pu, X. Yan, X. Pan, L. Zhang, Y. Wei, J. Gu, Atomically engineering activation sites onto metallic 1T-MoS2 catalysts for enhanced electrochemical hydrogen evolution, Nat. Commun. 10 (2019) 982.
[43] N. Feng, R. Meng, L. Zu, Y. Feng, C. Peng, J. Huang, G. Liu, B. Chen, J. Yang, A polymer-direct-intercalation strategy for MoS2/carbon-derived heteroaerogels with ultrahigh pseudocapacitance, Nat. Commun. 10 (2019) 1372.
[44] X. Huang, H. Xu, D. Cao, D. Cheng, Interface construction of P-Substituted MoS2 as efficient and robust electrocatalyst for alkaline hydrogen evolution reaction, Nano Energy 78 (2020), 105253.
[45] X. Hu, X. Tian, Y.-W. Lin, Z. Wang, Nickel foam and stainless steel mesh as electrocatalysts for hydrogen evolution reaction, oxygen evolution reaction and overall water splitting in alkaline media, RSC Adv. 9 (2019) 31563–31571.
[46] Y. Niu, W. Li, X. Wu, B. Feng, Y. Yu, W. Hu, C.M. Li, Amorphous nickel sulfide nanosheets with embedded vanadium oxide nanocrystals on nickel foam for efficient electrochemical water oxidation, J. Mater. Chem. A. 7 (2019) 10534–10542.
[47] H. Xu, B. Fei, G. Cai, Y. Ha, J. Liu, H. Jia, J. Zhang, M. Liu, R. Wu, Boronization-induced ultrathin 2D nanosheets with abundant crystalline–amorphous phase boundary supported on nickel foam toward efficient water splitting, Adv. Energy Mater. 10 (2020), 1902714.
[48] T. Shinagawa, A.T. Garcia-Esparza, K. Takanabe, Insight on tafel slopes from a microkinetic analysis of aqueous electrocatalysis for energy conversion, Sci. Rep. 5 (2015), 13801.
[49] Z.M. Hu, H. Nakatsuji, Adsorption and disproportionation reaction of OH on Ag surfaces: dipped adcluster model study, Surf. Sci. 425 (1999) 296–312.

[50] T. Kou, S. Wang, J.L. Hauser, M. Chen, S.R.J. Oliver, Y. Ye, J. Guo, Y. Li, Ni foam-supported Fe-Doped β-Ni(OH) 2 nanosheets show ultralow overpotential for oxygen evolution reaction, ACS Energy Lett. 4 (2019) 622–628.
[51] F. Song, X. Hu, Exfoliation of layered double hydroxides for enhanced oxygen evolution catalysis, Nat. Commun. 5 (2014) 4477.
[52] Y. Cui, Y. Xue, R. Zhang, J. Zhang, X. Li, X. Zhu, Vanadium-cobalt oxyhydroxide shows ultralow overpotential for the oxygen evolution reaction, J. Mater. Chem. A. 7 (2019) 21911–21917.
[53] D. Voiry, M. Chhowalla, Y. Gogotsi, N.A. Kotov, Y. Li, R.M. Penner, R.E. Schaak, P. S. Weiss, Best practices for reporting electrocatalytic performance of nanomaterials, ACS Nano 12 (2018) 9635–9638.
[54] V.D. Jović, B.M. Jović, EIS and differential capacitance measurements onto single crystal faces in different solutions: Part I - Ag(111) in 0.01 M NaCl, J. Electroanal. Chem. 541 (2003) 1–11.
[55] P.F. Liu, S. Yang, L.R. Zheng, B. Zhang, H.G. Yang, Mo6+ activated multimetal oxygen-evolving catalysts, Chem. Sci. 8 (2017) 3484–3488.
[56] M. Jahan, Q. Bao, K.P. Loh, Electrocatalytically active graphene-porphyrin MOF composite for oxygen reduction reaction, J. Am. Chem. Soc. 134 (2012) 6707–6713.
[57] S.V. Prabhakar Vattikuti, P.C. Nagajyothi, K.C. Devarayapalli, K. Yoo, N. Dang Nam, J. Shim, Hybrid Ag/MoS2 nanosheets for efficient electrocatalytic oxygen reduction, Appl. Surf. Sci. 526 (2020), 146751.
[58] N.R. Elezović, B.M. Babić, L.J.M. Vračar, N.V. Krstajić, Oxygen reduction at platinum nanoparticles supported on carbon cryogel in alkaline solution, J. Serb. Chem. Soc. 72 (2007) 699–708.
[59] M. Taleb, J. Nerut, T. Tooming, T. Thomberg, E. Lust, Oxygen electroreduction on platinum nanoparticles activated electrodes deposited onto d-glucose derived carbon support in 0.1 M KOH, J. Electrochem. Soc. 163 (2016) F1251–F1257.
[60] S. Fletcher, Tafel slopes from first principles, J. Solid State Electrochem 13 (2009) 537–549.
[61] A. Damjanovic, M.A. Genshaw, J.O. Bockris, Distinction between intermediates produced in main and side electrodic reactions, J. Chem. Phys. 45 (1966) 4057–4059.
[62] N.S. Georgescu, A.J.J. Jebaraj, D. Scherson, A critical assessment of XH2 O2 as a figure of merit for oxygen reduction electrocatalysts in aqueous electrolytes, ECS Electrochem. Lett. 4 (2015) F39–F42.
[63] X. Ge, A. Sumboja, D. Wuu, T. An, B. Li, F.W.T. Goh, T.S.A. Hor, Y. Zong, Z. Liu, Oxygen reduction in alkaline media: from mechanisms to recent advances of catalysts, ACS Catal. 5 (2015) 4643–4667.
[64] C.C.M. Neumann, E. Laborda, K. Tschulik, K.R. Ward, R.G. Compton, Performance of silver nanoparticles in the catalysis of the oxygen reduction reaction in neutral media: Efficiency limitation due to hydrogen peroxide escape, Nano Res. 6 (2013) 511–524.
[65] V.S. Bagotskii, L.N. Nekrasov, N.A. Shumilova, Electrochemical reduction of oxygen, Russ. Chem. Rev. 34 (1965) 717–730.
[66] K. Hsueh, Electrode kinetics of oxygen reduction a theoretical and experimental analysis of the rotating ring-disc electrode method, J. Electroanal. Chem. 153 (1983) 79–95.